AD-A119 861 AIR FORCE GEOPHYSICS LAB HANSCOM AFB MA F/G 4/1
A GLOBAL THERMOSPHERIC DENSITY MODEL BASED ON SATELLITE ACCELER--ETC(U)
JAN 82 F A MARCOS, D F GILLETTE, E C ROBINSON
UNCLASSIFIED AFGL-TR-82-0025 NL

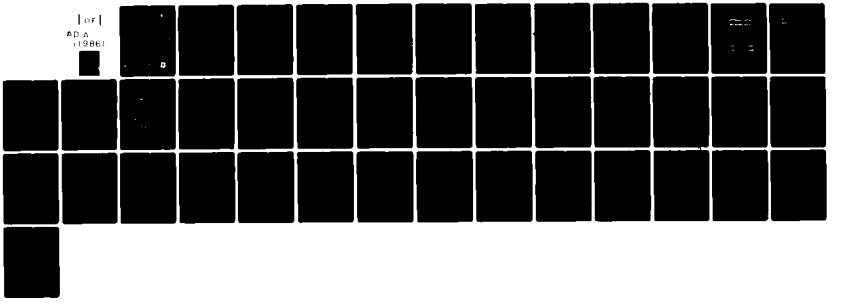

AFGL-TR-82-0025
ENVIRONMENTAL RESEARCH PAPERS, NO. 788

A Global Thermospheric Density Model Based on Satellite Accelerometer Data

FRANK A. MARCOS
DOROTHY F. GILLETTE
EDWARD C. ROBINSON

26 January 1982

AERONOMY DIVISION PROJECT 6690
AIR FORCE GEOPHYSICS LABORATORY
HANSCOM AFB, MASSACHUSETTS 01731

AIR FORCE SYSTEMS COMMAND, USAF

Unclassified

SECURITY CLASSIFICATION OF THIS PAGE (When Data Entered)

REPORT DOCUMENTATION PAGE		READ INSTRUCTIONS BEFORE COMPLETING FORM
1 REPORT NUMBER AFGL-TR-82-0025	2 GOVT ACCESSION NO. AD-A129 862	3 RECIPIENT'S CATALOG NUMBER
4 TITLE (and Subtitle) A GLOBAL THERMOSPHERIC DENSITY MODEL BASED ON SATELLITE ACCELEROMETER DATA		5 TYPE OF REPORT & PERIOD COVERED Scientific. Interim. 6 PERFORMING ORG. REPORT NUMBER ERP, No. 766
7 AUTHOR(s) Frank A. Marcos Dorothy F. Gillette Edward C. Robinson		8 CONTRACT OR GRANT NUMBER(s)
9 PERFORMING ORGANIZATION NAME AND ADDRESS Air Force Geophysics Laboratory (LKB) Hanscom AFB Massachusetts 01731		10 PROGRAM ELEMENT, PROJECT, TASK AREA & WORK UNIT NUMBERS PE 62101 F 66900403
11 CONTROLLING OFFICE NAME AND ADDRESS Air Force Geophysics Laboratory (LKB) Hanscom AFB Massachusetts 01731		12 REPORT DATE 26 January 1982 13 NUMBER OF PAGES 42
14 MONITORING AGENCY NAME & ADDRESS(if different from Controlling Office)		15 SECURITY CLASS. (of this report) Unclassified 15a DECLASSIFICATION DOWNGRADING SCHEDULE

16 DISTRIBUTION STATEMENT (of this Report)

Approved for public release; distribution unlimited.

17 DISTRIBUTION STATEMENT (of the abstract entered in Block 20, if different from Report)

18 SUPPLEMENTARY NOTES

19 KEY WORDS (Continue on reverse side if necessary and identify by block number)

Satellites	Thermospheric density variations
Accelerometers	Thermospheric model evaluation
Atmospheric density	Multiple regression modelling
Atmospheric models	Neutral atmospheric data base
Aerodynamic drag data	

20 ABSTRACT (Continue on reverse side if necessary and identify by block number)

Measurements from the accelerometer experiments on four low-altitude satellites (S3-1 and Atmosphere Explorer-C, -D, and -E) have been combined to produce an empirical model of the neutral mass density from 140 to 240 km. Data from over 8000 orbits are analyzed using the least-squares method of multiple linear regression. The resulting model gives density as a function of solar flux (for flux values 60 to 130 units), geomagnetic activity, day of year, local time, latitude and altitude. It provides a more accurate fit to the measured data than other available atmospheric models. Three

DD FORM 1 JAN 73 1473 EDITION OF 1 NOV 65 IS OBSOLETE

Unclassified

SECURITY CLASSIFICATION OF THIS PAGE (When Data Entered)

20. Abstract (Continued)

commonly used models are evaluated by comparison of their predicted density variations with those of this empirical model.

Preface

The authors are indebted to Robert W. Fioretti, Andrew J. Mazzella, Jr., Rebecca Leong, and Wendell Smith, RDP Inc., for the extensive accelerometer data analysis effort, including development and implementation of the multiple regression program and the contour plotting routines under AF Contract F19628-79-C-0117; to James N. Bass, Logicon, Inc., for providing atmospheric model data; to K.S.W. Champion and J.M. Forbes for critically reviewing the manuscript, and to Margaret Anderson and Stephanie Furlow for typing the draft and final manuscript.

Contents

Illustrations

Tables

A Global Thermospheric Density Model Based on Satellite Accelerometer Data

1. INTRODUCTION

Extensive measurements of the lower thermosphere neutral density have been derived from the accelerometers on the Atmosphere Explorer -C, -D, and -E, and S3-1 satellites. An empirical Accelerometer Density Model (ADM) has been developed from these data. This model permits organization of the large density data base in a form suitable for geophysical interpretation and for comparison with other data. As in previous studies,[1,2,3] the least-squares method of multiple linear regression is used to extract and analyze the density data. Density variations in the altitude region 140 to 240 km are represented as a function of geomagnetic activity, latitude, local time, day of year and solar flux ($60 \leq F \leq 130$ units). The major advantage of the present model is improved formulations for the latitude variations in geomagnetic activity, local time and semiannual effects.

(Received for publication 13 January 1982)

1. Forbes, J.M., and Garrett, H.B. (1975) Variations in the atmospheric neutral density at 145 km, Planet. Space Sci. 23:1399.

2. Marcos, F.A., Garrett, H.B., Champion, K.S.W., and Forbes, J.M. (1977) Density variations in the lower thermosphere from analysis of the AE-C accelerometer measurements, Planet. Space Sci. 25:499.

3. Marcos, F.A., and Champion, K.S.W. (1979) Empirical model of lower thermospheric density for low solar flux and quiet geomagnetic conditions, Space Research 19:89.

Knowledge of atmospheric density variability is required for satisfactory design, operation, and orbit prediction of low-altitude AF mission satellites. Existing models of the lower thermosphere, particularly below 250 km, are deficient since they are primarily based on data at higher altitudes. Physical and mathematical difficulties limit extrapolation of these data to lower altitudes; namely, the assumption of diffusive equilibrium is not always valid, and the lower thermosphere boundary conditions are poorly known and variable. This report compares the ADM results with the three most commonly used models: J71,[4] J77,[5] and MSIS.[6] Results of this study provide a quantitative estimate of improvements required in properties of current thermospheric models in order to account for the observed variations. Additional low-satellite altitude accelerometer data obtained during moderate and high solar flux conditions are becoming available.[7,8] These results will be utilized in order to extend the present formulations to all solar flux conditions.

2. DATA SELECTION AND COVERAGE

Table 1 summarizes orbital characteristics and dates of acquisition for each satellite. Marcos et al[9] have provided a complete description of the experiments and the data base. Over three million density measurements were obtained. This amount is too large to handle practically and much larger th n required to define the parameters to be fitted. Therefore, a data base was constructed by selecting values at 5-km intervals from 140 to 240 km. At each 5-km interval, the density

4. Jacchia, L.G. (1971) Revised Static Models of the Thermosphere and Exosphere with Empirical Temperature Profiles, Spec. Rept. 332, Smithsonian Astrophys. Observatory, Cambridge, Massachusetts.

5. Jacchia, L.G. (1977) Thermospheric Temperature Density and Composition: New Models, Special Rept. 375, Smithsonian Astrophys. Observatory, Cambridge, Massachusetts.

6. Hedin, A.E., Salah, J.E., Evans, J.V., Reber, C.A., Newton, G.P., Spencer, N.W., Kayser, D.C., Alcayde, D., Bauer, P., Cogger, L., and McClure, J.P. (1977) A global thermospheric model based on mass spectrometer and incoherent scatter data, MSIS 1, N_2 density and temperature, J. Geophys. Res. 82:2139.

7. Marcos, F.A., and Champion, K.S.W. (1979) Satellite Density Measurements with a Rotatable Calibration Accelerometer (ROCA), AFGL-TR-79-0005, ADA 069740.

8. Marcos, F.A., and Swift, E.R. (1981) Application of the Satellite Triaxial Accelerometer to Atmospheric Density and Wind Studies, AFGL-TR-82-0091.

9. Marcos, F.A., McInerney, R.E., and Fioretti, R.W. (1978) Variability of the Lower Thermosphere Determined from Satellite Accelerometer Data, AFGL-TR-78-0134, ADA 058982, Air Force Geophysics Laboratory, Hanscom AFB, Massachusetts.

Table 1. Satellite Orbital Characteristics and Data Acquisition Periods

Satellite	Launch	End Elliptical Data Acquisition	Inclination (degrees)	Initial Perigee (km)	Initial Apogee (km)
AE-C	Dec 73	Nov 74	68°	156	4000
S3-1	Oct 74	May 75	97°	160	4000
AE-D	Oct 75	Jan 76	90°	156	3800
AE-E	Nov 75	Nov 76	20°	157	3000

value was selected using a second-order fit to three points: the one closest to the 5-km altitude step and the two adjacent points. As a result, data from the four satellites are represented by 148,000 density values.

Typical results from the data base, namely, individual density values at 180 km, are shown versus day of year in the second from the top frame of Figure 1a, b, and c. The 10.7-cm solar flux, ratio to the J71 model and the 3-hr planetary K_p index are also given. The 1974 data (Figure 1a) are from AE-C (1 January to 30 October), and from AE-C and S3-1 (31 October to 31 December). The 1975 data (Figure 1b) are from S3-1 to 15 May; from AE-D (13 October to 6 December), and from AE-D and AE-E (7 December to 31 December). The 1976 data (Figure 1c) are from AE-D and AE-E to 30 January, and from AE-E alone to 15 November. Distribution of the complete data base as a function of day of year, altitude, latitude, local time, solar flux and geomagnetic activity has been given by Marcos et al[9] for each individual satellite data set. They are summarized and discussed briefly here, with all four sets of data combined.

The distribution of data points with altitude is shown in Figure 2a. Data below 150 km were obtained only during the AE-C and AE-E perigee-lowering maneuvers. The latitude distribution (Figure 2b) peaks between ± 20° (41 percent of data base) because of the contribution of the AE-E data. However, there are 56,000 points from 20° to 60°| and 31,000 points from |60° to 90°|. These are adequate to permit analysis of latitudinal variations in density. Excellent local time coverage was provided by AE-C and -E, whereas AE-D and S3-1 data were mainly confined to local times near 2200 hours and 0800 hours (Figure 2c). Data were obtained during the declining portion of solar cycle 20 and the beginning of solar cycle 21. Figure 2d shows that flux values greater than 100 were exceeded only 4 percent of the time. A wide range of geomagnetic conditions was encountered (see Figure 2e). Geomagnetically active conditions (assuming $K_p > 3$) occur for 40 percent of the data. Latitudinal coverage as a function of day of year is shown in Figure 3. Position of the upleg and downleg latitude for data at the typical altitude

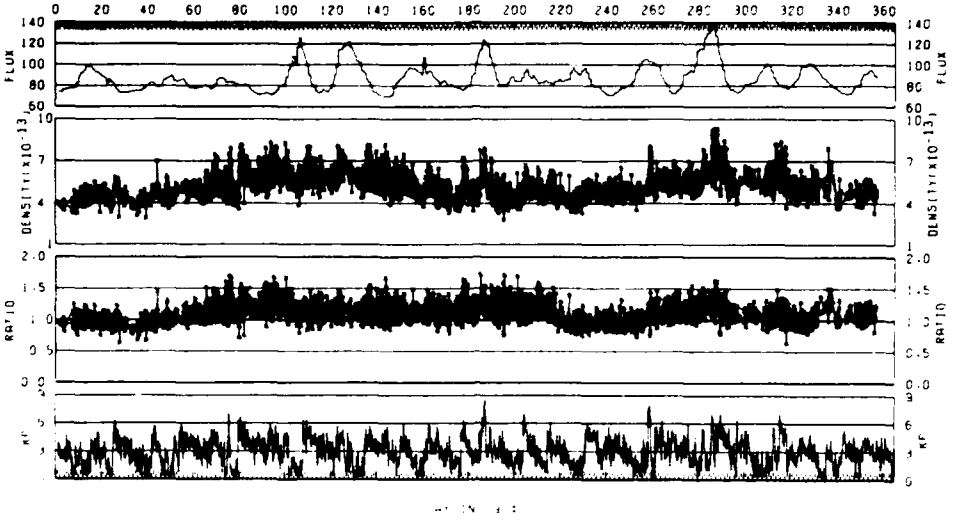

Figure 1a. Accelerometer Data Base at 180 km for 1974. Latitude, density (g/cm^3), ratio to J71 model and K_p as a function of time

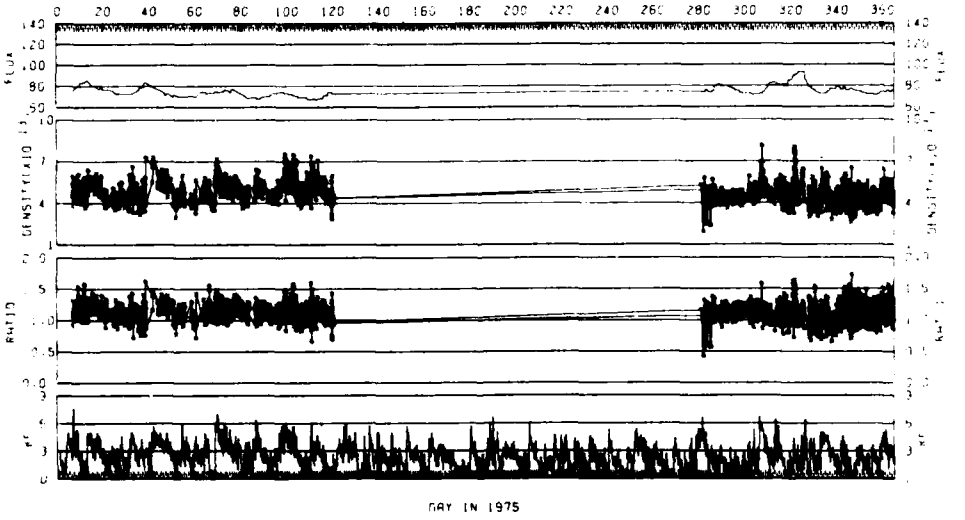

Figure 1b. Accelerometer Data Base at 180 km for 1975. Latitude, density (g/cm^3), ratio to J71 model and K_p as a function of time

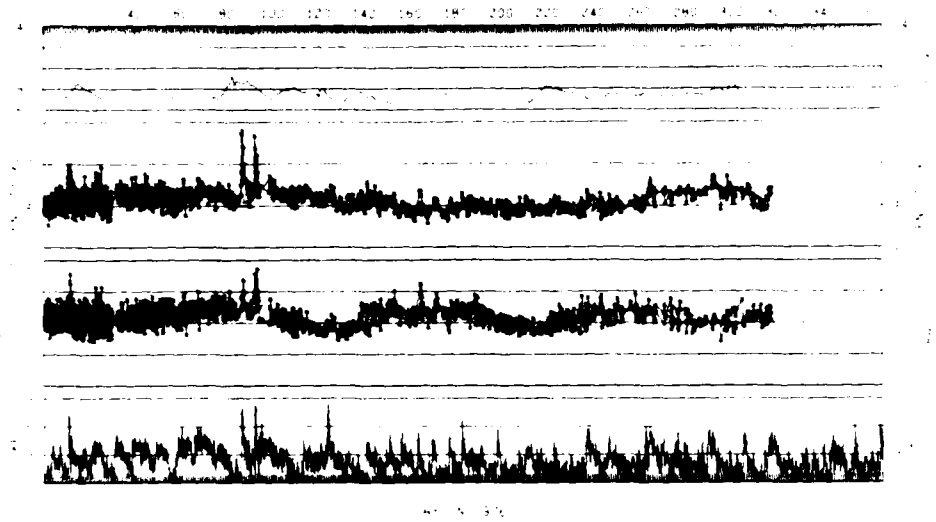

Figure 1c. Accelerometer Data Base at 180 km for 1976. Latitude, density (g/cm^3), ratio to J71 model and K_p as a function of time

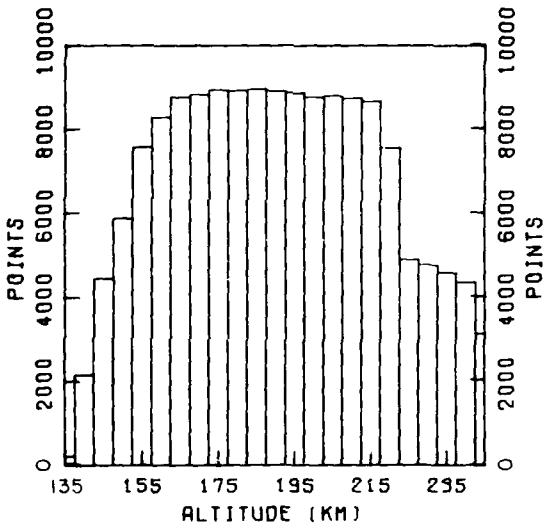

Figure 2a. Histogram of Data Distribution as a Function of Altitude

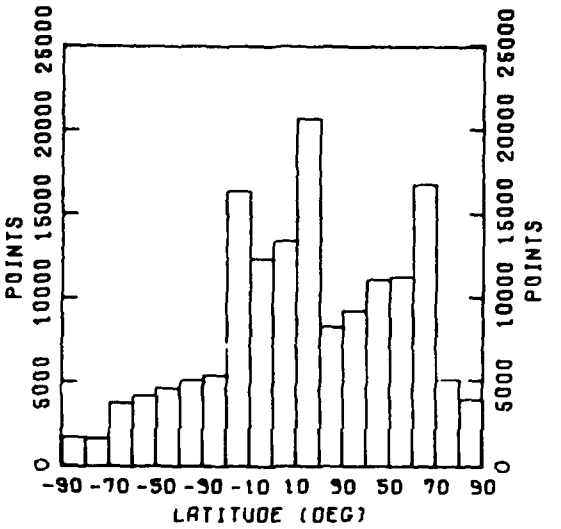

Figure 2b. Histogram of Data Distribution as a Function of Geographic Latitude

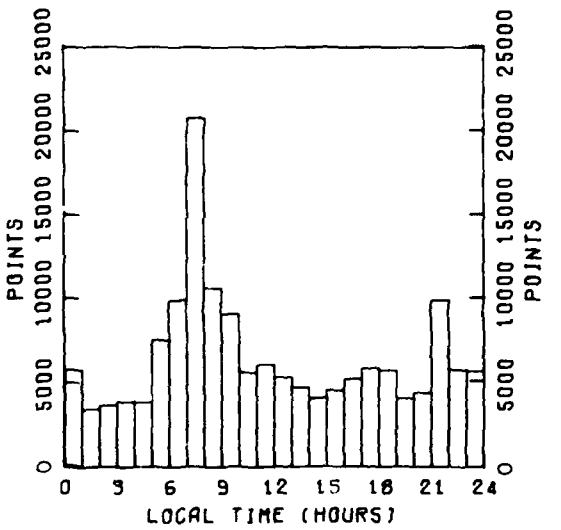

Figure 2c. Histogram of Data Distribution as a Function of Local Time

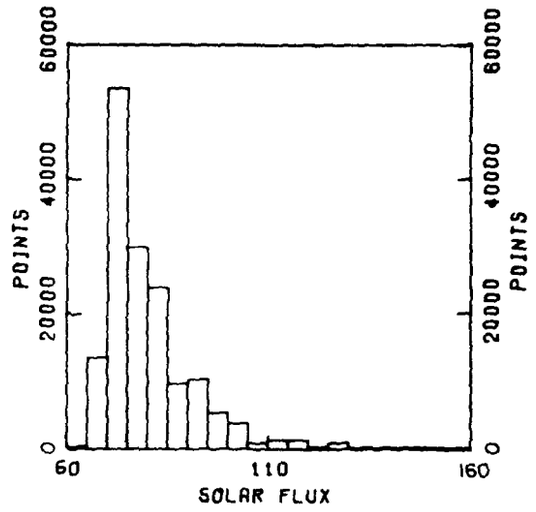

Figure 2d. Histogram of Data Distribution as a Function of Solar Flux

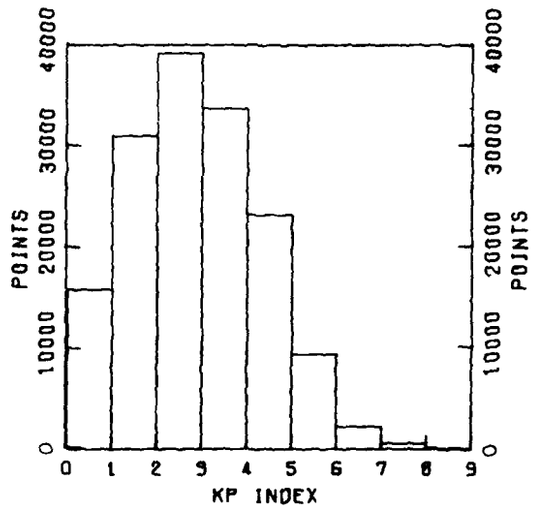

Figure 2e. Histogram of Data Distribution as a Function of Geomagnetic Activity

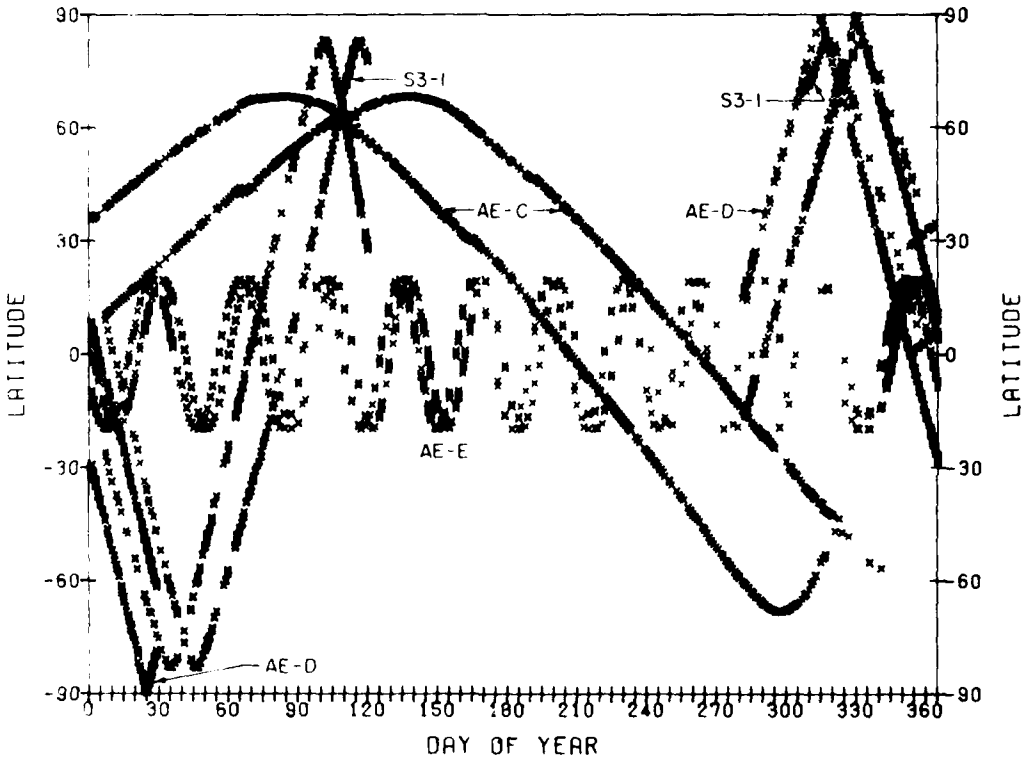

Figure 3. Distribution of Input Data at 200 km for Density Model in Geographic Latitude vs Day of Year Coordinates

of 200 km is shown for each satellite. Coverage from AE-E is evident as the data points cycling between $\pm 20^{o}$. Atmosphere Explorer-D provides measurements extending to high latitudes for northern hemisphere winter and southern hemisphere summer conditions; S3-1 follows a similar track but continues to northern hemisphere spring conditions. The AE-C data include the high latitude northern hemisphere spring and southern hemisphere fall conditions.

One advantage of this data set is that all measurements were obtained by the same technique and have essentially the same accuracy (see Section 4.5). Hence no one satellite data set will have undue weighting influence on the fit of specific parameters.

3. FORMULATION OF THE ACCELEROMETER DENSITY MODEL (ADM)

A multiple linear regression model is used to approximate the dependent variable, atmospheric density by a linear combination of independent variables. The independent variables considered in this study (at each 5-km interval) are the variations associated with solar flux, geomagnetic activity, day of year, local time, and latitude. Terms were chosen to represent known atmospheric variations in a relatively simple manner. All latitude dependencies are described in geographic coordinates. Test runs indicated that the fit to the data was not sufficiently improved to warrant the complexity of a combination of geographic and geomagnetic coordinates.

Table 2 contains a list of the independent variables. Variations related to solar activity are approximated by the 81-day centered average of the observed 10.7-cm solar radio flux ($\bar{F}_{10.7}$) and by the difference $F_{10.7} - \bar{F}_{10.7}$ using a one day lag for the daily $F_{10.7}$ value. Geomagnetic activity variations are represented, respectively, by the average of the four 3-hr K_p values ($\bar{K}_{p12}$) and the eight K_p values ($\bar{K}_{p24}$) that occurred before the time of the density measurements, by a latitude dependence for $\bar{K}_{p12}$, by K_p with a 6-hr lag (K_{p6}), and by a latitude-dependent time lag. This lag, derived by correlation analysis of data in 15^{o} latitude intervals is of the form:

$$K_p \Delta t = 3 + \frac{1}{12} \left| |\theta| - 60 \right| \text{ hours} \qquad (1)$$

where θ = geographic latitude. This is an average result. The response time is believed overestimated, since data are not available on a continuous basis, or even on an every-orbit basis, and the measurements are not always in the localized region of initial heating. The latter situation will particularly overestimate the high-latitude time delay. However, Eq. (1) is consistent with the measured data.

Table 2. Terms Used in Regression Analysis

1.	$\overline{F}_{10.7}$	Solar Flux
2.	$F_{10.7} - \overline{F}_{10.7}$	
3.	$\overline{K}_{p12}$	Geomagnetic Activity
4.	$\overline{K}_{p24}$	
5.	K_{p6}	
6.	$\text{Cos } \theta \, \overline{K}_{p12}$	
7.	$\text{Sin } \theta \, \overline{K}_{p12}$	
8.	$K_p \Delta t$	
9.	$\cos \omega t + \phi_1$	Local Time
10.	$\cos 2\omega t + \phi_2$	
11.	$\cos 3\omega t + \phi_3$	
12.	$\cos \theta \, (\cos \omega t + \phi_4)$	
13.	$\sin \theta \, (\cos \omega t + \phi_5)$	
14.	$\cos \theta \, (\cos 2\omega t + \phi_6)$	
15.	$\sin \theta \, (\cos 2\omega t + \phi_7)$	
16.	$\cos \theta \, (\cos 3\omega t + \phi_8)$	
17.	$\sin \theta \, (\cos 3\omega t + \phi_9)$	
18.	$\cos \chi_{ss}$	
19.	$\cos \alpha t + \phi_{10}$	Day of Year
20.	$\cos 2\alpha t + \phi_{11}$	
21.	$\sin \theta \, (\cos \alpha t + \phi_{12})$	
22.	$\sin \theta \, (\cos 2\alpha t + \phi_{13})$	
23.	$\lvert \theta \rvert$	Latitude

Variations associated with day of year are represented by sine and cosine functions having periods of 1 and 1/2 year and a nonsymmetric latitude dependence. Local time effects are represented by terms of the form $\cos (n\omega t) + \phi$ where ϕ = phase and $n = 1, 2, 3$ and by latitude-dependent components of the form $(\cos \theta) \cos n\omega t$ and $(\sin \theta) \cos n\omega t$. Also a $\cos \chi_{ss}$ term was used to represent a subsolar bulge with:

$$\cos \chi_{ss} = \cos \theta \cos t \cos \delta + \sin \theta \sin \delta \qquad (2)$$

where

χ = solar zenith angle

θ = latitude

t = local time

δ = solar declination angle.

A pure latitude variation was included by the absolute value of the satellite geographic latitude.

4. RESULTS

With use of the terms in Table 2, the stepwise multiple linear regression analysis was carried out for each 5-km interval data set between 140 and 240 km. As in previous analyses, for example, Forbes and Garrett,[1] the process of adding terms in each case was terminated when the Student's t-value fell below the 95 percent confidence level. Results for successive applications of the regression analysis to data at 200 km are given in Table 3. This table lists the functions (F_i) in order of entry into the regression analysis, regression coefficient (a_i), their standard deviations (σ_i), and the correlation coefficients (R) for the final regression equation. Although there are altitudinal differences in the relative importance and the entry of some of the coefficients, the 200-km data were selected as being typical. Density values are calculated by:

$$\rho = a_o + \Sigma_i a_i F_i \qquad (3)$$

4.1 Solar Activity Variations

The major energy source affecting the thermosphere is the solar ultraviolet flux between 30 and 2400 A. The global mean heating due to the solar EUV heat source is about 4×10^{18} erg·sec^{-1} above 120 km and 10^{19} erg·sec^{-1} above 100 km. A correlation of density with the 10.7-cm radio flux monitored at NRC Ottawa, Canada is a feature of all current models. This correlation does not necessarily represent the complex physical mechanisms of the interactions between the solar EUV flux and the thermosphere. However, since $F_{10.7}$ is found to reflect variations in the thermospheric energy input, it provides a readily available but imperfect indicator of solar activity.

The density response to the average solar flux $\bar{F}$ in the empirical model (ADM) is examined by letting $F = \bar{F}$ (so that $F - \bar{F} = 0$). For a unit increase in $\bar{F}$ the data

Table 3. Regression Analysis Results at 200 km

i	F_i	a_i	σ_i	R
1.	$\overline{K}_{p12}$	1.544 E-14	9.962 E-16	0.5449
2.	$\overline{F}_{10.7}$	2.063 E-15	5.251 E-17	0.6473
3.	$\cos(2\alpha + 109.30)$	2.045 E-14	4.569 E-16	0.7091
4.	$\sin\theta \cos(\alpha + 159.34)$	2.519 E-14	7.210 E-16	0.7376
5.	$F_{10.7} - \overline{F}_{10.7}$	9.033 E-16	3.441 E-17	0.7548
6.	$\cos\theta \cos(\omega t + 14.94)$	1.526 E-14	6.409 E-16	0.7720
7.	$\cos(\alpha + 28.25)$	1.144 E-14	5.234 E-16	0.7876
8.	$\overline{K}_{p24}$	6.298 E-15	6.407 E-16	0.7901
9.	$\sin\theta \cos(2\omega t + 0.70)$	1.958 E-15	8.190 E-16	0.7922
10.	$\cos\theta \cos(3\omega t + 4.17)$	8.710 E-15	1.468 E-15	0.7930
11.	$\sin\theta \cos(2\alpha + 48.10)$	1.911 E-15	8.217 E-16	0.7937
12.	$\cos\theta \overline{K}_{p12}$	-8.095 E-15	7.970 E-16	0.7942
13.	$\lvert\theta\rvert$	-2.001 E-16	2.758 E-17	0.7968
14.	$\cos(3\omega t + 0.38)$	4.706 E-15	1.173 E-15	0.7972
15.	$K_p \Delta t$	1.187 E-15	4.654 E-16	0.7977
16.	$\sin\theta \overline{K}_{p12}$	-9.652 E-16	1.958 E-16	0.7978
17.	$\cos(2\omega t + 1.28)$	1.859 E-14	1.504 E-15	0.7980
18.	$\cos\theta \cos(2\omega t + 7.19)$	2.090 E-14	1.761 E-15	0.8012
19.	$\sin\theta \cos(\omega t + 0.81)$	3.422 E-15	8.185 E-16	0.8014
20.	$\cos(\omega t + 10.54)$	1.588 E-15	4.636 E-16	0.8017

θ = geographic latitude

$\omega = 2\pi/24$

$\alpha = 2\pi/365.2$

local time phases are in hours

day of year phases are in days

a_o = 1.722 E-14

analysis indicates a density increase varying from 0.25 percent at 140 km to 1.50 percent at 240 km. These computations are made for the March equinox (day 81) at the equator with local time = 1500 hours and K_p = 0. These default values are used in the remainder of this section. The ADM results are represented by the solid straight line in Figure 4; also shown are the J71, J77, and MSIS increases per unit $\bar{F}$ increase computed at 20-km intervals. At 140 km the MSIS value, not shown on the plot, is -0.04 percent (a density decrease is predicted). At all altitudes the ADM shows the largest response to $\bar{F}$. The J77 model response is about 0.1 percent lower, showing the closest agreement. The actual mass density values as a function of $\bar{F}$ are shown for the altitude of 200 km in Figure 5. Note that the ADM has the lowest density value at $\bar{F}$ = 60. For the range $\bar{F}$ = 60 to 130 units, the average density increases per unit F are 1.08 percent (ADM), 0.98 percent (J77), 0.83 percent (J71) and 0.72 percent (MSIS).

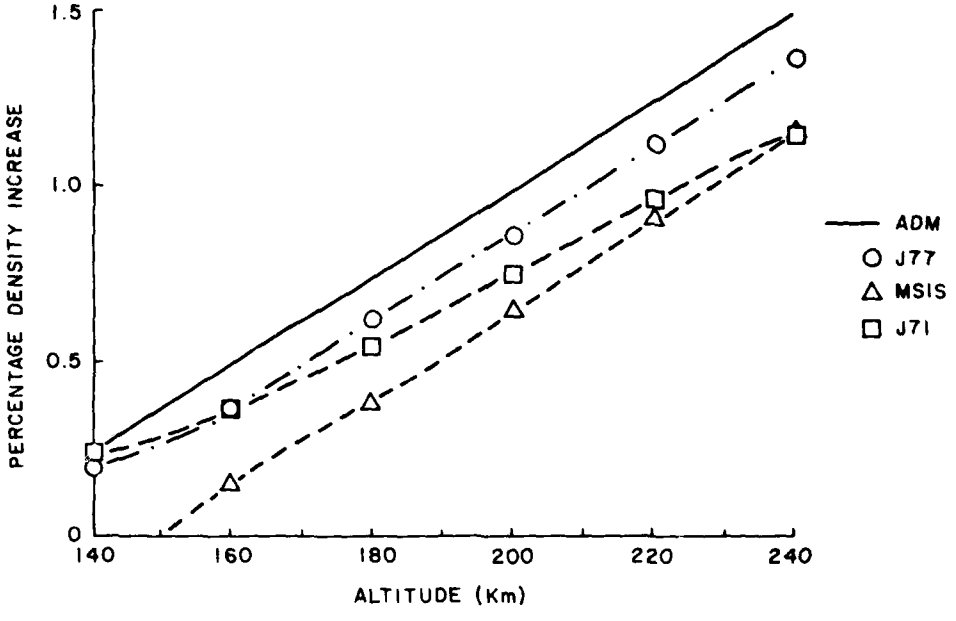

Figure 4. Percentage Density Increase per Unit Increase in Average Solar Flux ($\bar{F}$) Plotted vs Altitude (Day = 81, LT = 1500 hr, Latitude = 0, K_p = 0, F = 75)

Density variability at 200 km with respect to the daily solar flux, F, is examined in Figure 6. For this case, F varies from 60 to 130 units whereas $\bar{F}$ is held constant at 75 units. (Again the ADM has the lowest density values for low values of F.) The ADM increases by 0.45 percent per F unit. The other three

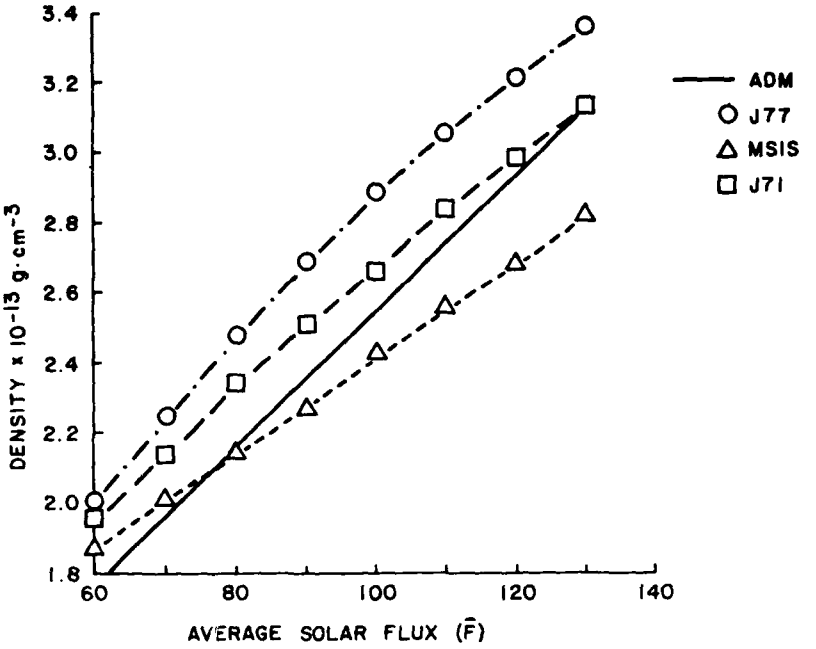

Figure 5. Density Variations at 200 km as a Function of the Mean Solar Decimetric Flux $\bar{F}$, for Day = 81, LT = 1500 hr, Latitude = 0^{o} and $K_p = 0$

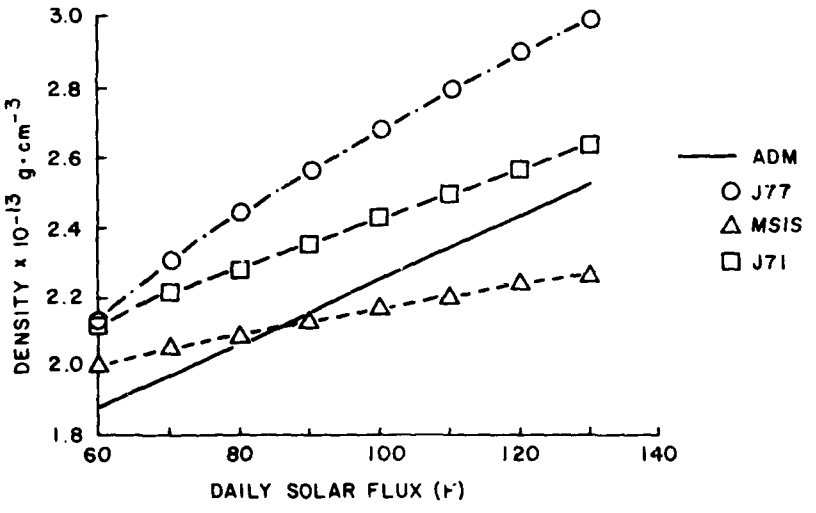

Figure 6. Density Variations at 200 km as a Function of $F-\bar{F}$; for $\bar{F} = 75$, Day = 81, LT = 1500 hr, Latitude = 0^{o} and $K_p = 0$

models give the values 0.57 percent (J77), 0.32 percent (J71), and 0.18 percent (MSIS). For this case, the ADM data predict a variation that is about halfway between the J77 and J71 model values.

It is pointed out that these results are obtained during the declining portion of solar cycle 20 and the beginning of solar cycle 21. Linear extrapolation of the present model to higher solar flux conditions may not be valid. This can be examined with ROCA[7] and SETA[8] data. Also, Hinteregger[10] has shown that solar EUV radiation correlates more closely with $F_{10.7}$ during solar cycle 21 than it did for solar cycle 20. Therefore, in any model, caution is required in basing density predictions on results derived from a different solar cycle. This emphasizes the need for a solar activity index based on direct determination of the solar EUV heating.

4.2 Geomagnetic Variations

Rapid global fluctuations in density with a typical duration of one to several days are connected with geomagnetic variations. The energy input results from solar wind/earth's magnetic field interactions and involves Joule heating and particle precipitation along magnetic field lines. During geomagnetically quiet conditions, the energy input due to these high latitude processes is of the order 5×10^{17} erg · sec^{-1}. This energy input can increase by a factor of 10 or more during large geomagnetic storms. The planetary 3-hr K_p index used as an indicator of geomagnetic activity does not necessarily represent physical mechanisms responsible for density variations. It is derived from a network of poorly distributed magnetometer stations (ten between 43 and 60°N and two between 37 and 43°S). Hence it is particularly limited when describing data at high or low latitudes. As with $F_{10.7}$, however, K_p is presently the only index available for systematic geomagnetic activity correlations.

All models show similar trends that are associated with geomagnetic storms. The amplitude of the density increase generally depends on the strength of the geomagnetic storm as indicated by the K_p index. The atmospheric response occurs first at auroral zone latitudes and then at low latitudes, with a delay of typically 6 to 8 hours. This implies that the energy transferred to the thermosphere through auroral processes at high latitudes is distributed later through dynamic processes. Recent composition measurements and theoretical studies have shown that atmospheric winds driven by the high-latitude heat source are involved in global redistribution of energy and mass. This wind-induced diffusion at high latitudes results in a decrease in the light atmospheric constituents (O and He), whereas the heavy

10. Hinteregger, H.E. (1979) Development of solar cycle 21 observed in EUV spectrum and atmospheric absorption, J. Geophys. Res. 84:1933.

constituents (N_2 and A) increase in response to the temperature increase.[11] Consequently, the response of neutral density is expected to be latitude and composition dependent.

The density variations derived for the geomagnetic effect exhibit an altitude dependence. Figure 7 compares the increase in density per unit rise in K_p as a function of altitude predicted by the ADM and J71, J77, and MSIS models. Percentages are computed as 1/6 of the increase in density going from $K_p = 0$ to $K_p = 6$. The data are for $F = \bar{F} = 75$, day = 81, latitude = 0 and LT = 1500 hours. Regression analysis revealed increases from 4.4 percent at 140 km to 9.7 percent at 240 km for the ADM. On the whole, J71 gives closest agreement to this result. Both J71 and MSIS show less variability than ADM. However, J77 predicts a constant value of 11.7 percent at all altitudes. This is a consequence of partitioning the geomagnetic effect into three parts, with the "density wave" affecting the equatorial density. At higher latitudes, the J77 model predicts an altitude-dependent K_p response.

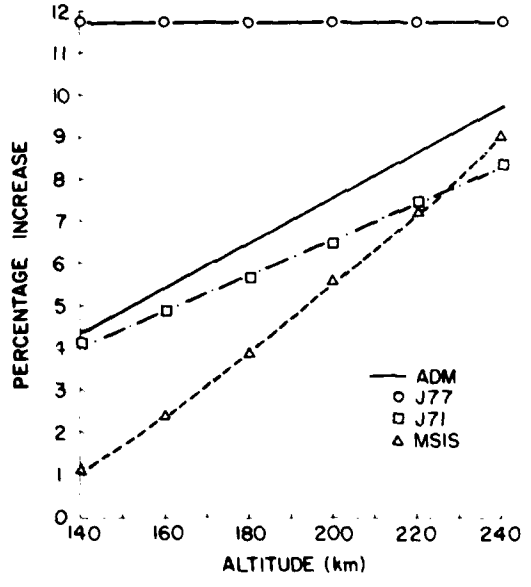

Figure 7. Percentage Density Increase per Unit K_p Increase as a Function of Altitude

11. Mayr, H.G., Harris, I., and Spencer, N.W. (1978) Some properties of upper atmosphere dynamics, Rev. Geophys. Space Phys. 16:539.

Figure 8 shows the increase in density at 200-km altitude as a function of K_p. At values of $K_p > 6$, the ADM values are shown as a dashed line. Extrapolation of a linear model is not valid at the high K_p values where the geomagnetic effect becomes highly nonlinear. (The low density value at $K_p = 0$ in the MSIS data is due to a continuity problem in the model rather than an assumed nonlinear effect.) Limitation of the ADM results to $K_p = 6$ only excludes about 1.5 percent of the K_p values experienced, based on the present data set and long-term occurrence probabilities.[12]

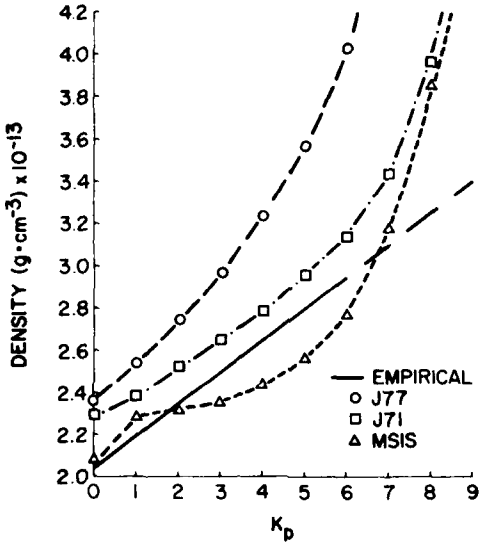

Figure 8. Density Variation at 200 km as a Function of K_p (Day = 81, LT = 1500 hr, Latitude = 0, $F = \bar{F} = 75$)

A significant latitude dependence was derived in the regression analysis. Figure 9 compares the percentage increase in density per unit K_p versus geographic latitude predicted by the various models. Data are presented for the altitude of 200 km. At the equator, the ADM enhancement is 7.3 percent; it increases to 13.1 percent at -90^o and to 11.4 percent at $+90^o$. The small pole-pole difference is within the standard deviation of each enhancement and cannot be unambiguously related to a hemispheric asymmetry in the geomagnetic effect. The shape of the ADM curve and its range of values agrees best with MSIS. Since higher order terms

12. Cage, A. L. and Zawalick, E. J. (1972) A Discussion of Geomagnetic Indices K_p and A_p, 1932 to 1971, AFCRL-72-0693, AD 756828.

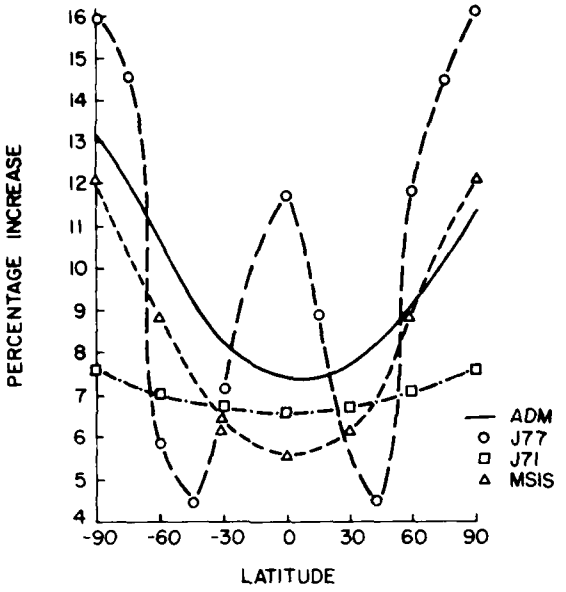

Figure 9. Percentage Density Increase per Unit K_p as a Function of Geographic Latitude

were not analyzed in the ADM formulation, it is not possible to evaluate the complicated J77 latitudinal response. Averaged over all latitudes, however, J77 agrees well with ADM.

At all altitudes, the term with the highest correlation coefficient was $\overline{K}_{p12}$. Table 3 shows that at 200 km this term accounted for 29.7 percent of the variation in the data. Regression analysis tends to smooth the short-term or transient variations in the data; examination of Figure 1 shows individual magnetic storm effects with response related to a specific jump in K_p. Statistical analyses (unpublished) of the present accelerometer data also indicate geomagnetic variations that are a function of local time, season, and hemisphere. These will be examined in a further study incorporating the more recent ROCA[7] and SETA[8] accelerometer results. A major limitation of all present models is their inability to predict accurately the phase and amplitude of geomagnetic variations. However, this difficulty is being alleviated by new analyses in both the MSIS[13, 14] and J77[15] models.

References 13 to 15 are listed on page 42.

4.3 Local Time Variations

Density structure as a function of local time has been extracted in previous studies of accelerometer density data. Marcos et al[9] statistically studied AE-E data at 160, 200, and 240 km, and found characteristics of atmospheric tides. At 160 km, two nearly equal maxima were observed near 0730 and 2300 hours respectively; at 240 km, a broad maximum was centered near 1400 hours. Forbes and Marcos[16] extended this AE-E analysis. They determined that the transition from predominantly semidiurnal to predominantly diurnal tidal effects occurs at 180 ±5 km and that a substantial summer/winter difference, consistent with the Forbes[17] model, occurs in the phase structure of the semidiurnal component of density. Using data from all four satellites, Forbes and Marcos[18] showed that the phase of the diurnal variation varies with latitude shifting to later local times from the equator to midlatitudes.

The ADM density structure as a function of local time is shown in Figures 10a, b, and c for the altitudes 160, 200, and 240 km, respectively. For each case, density values are calculated assuming day = 81, latitude = 0, $F = \bar{F} = 75$ and $K_p = 0$. In Figure 10a the ADM results show the dominance of the semidiurnal tide. This result is in remarkable agreement with MSIS. Table 4 shows that the phases of the maxima and minima for these models are within 1/2 hour for three cases and within one hour for the fourth case. Ratios of the morning and evening maxima to the early morning and afternoon minima are compared in Table 5. The ADM amplitudes are in the range 14.5 ± 1.5 percent, whereas those of MSIS are within 15.0 ± 1.5 percent. Both J71 and J77 show only a diurnal variation with their maximum (amplitude of about 29 percent) near 1500 hours. This time corresponds to near-minimum densities in ADM and MSIS. At 200 km (Figure 10b), ADM predicts a broad maximum between 1100 and 2000 hours as the diurnal variation becomes more prominent. This result agrees well with the MSIS local time behavior, but not with the well-defined diurnal bulges of the J71 and J77 models. For each model the ratio of maximum to minimum density is as follows: 1.20 (ADM), 1.15 (MSIS), 1.62 (J71), and 1.56 (J77). All models show the dominance of the diurnal tide at 240 km (Figure 10c). A phase of 1330 hours for the maximum is obtained for ADM. The J71 and J77 phases are at 1400 and 1530 hours, respectively, whereas the MSIS data maximize at 1600 hours. The amplitude of the ADM variation (1.54) is between that of the MSIS (1.26) and the J71 (1.97) and J77 (1.95) models. Based on the

16. Forbes, J. M., and Marcos, F. A. (1979) Tidal variations in total mass density as derived from the AE-E Mesa experiment, J. Geophys. Res. 84:31.

17. Forbes, J. M. (1978) Tidal variations in O, O_2, N_2, Ar, He and H, J. Geophys. Res. 83:3691.

18. Forbes, J. M., and Marcos, F. A. (1980) Seasonal-latitudinal tidal structures of O, N_2 and total mass density in the thermosphere, J. Geophys. Res. 85:3489.

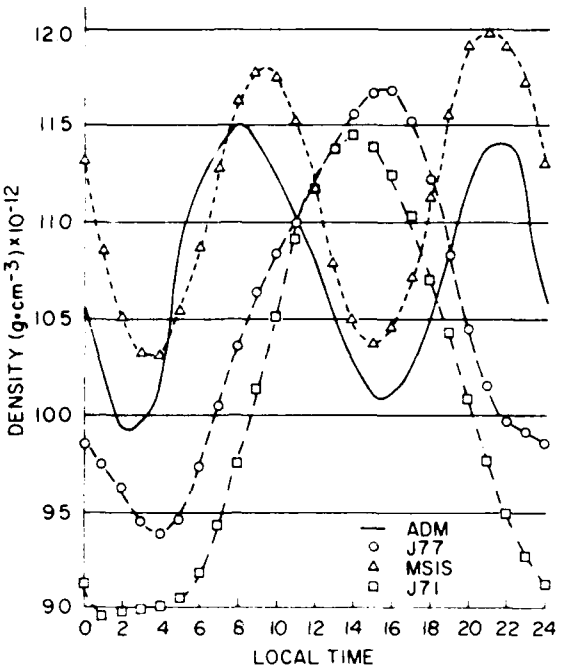

Figure 10a. Density Variation at 160 km as a Function of Local Time (Day = 81, Latitude = 0, $F = \bar{F} = 75$, $K_p = 0$)

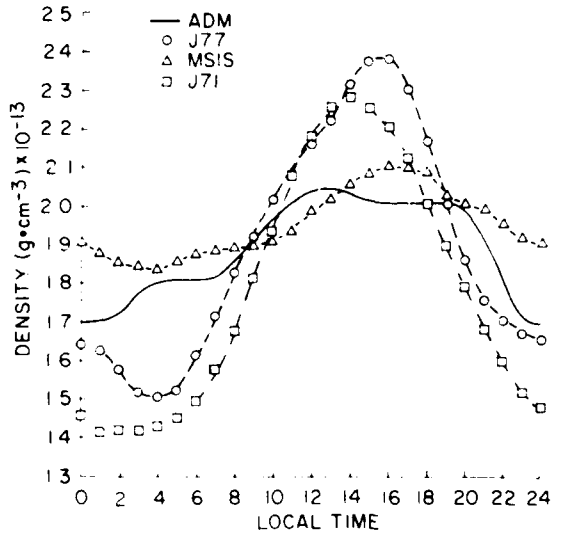

Figure 10b. Density Variation at 200 km as a Function of Local Time

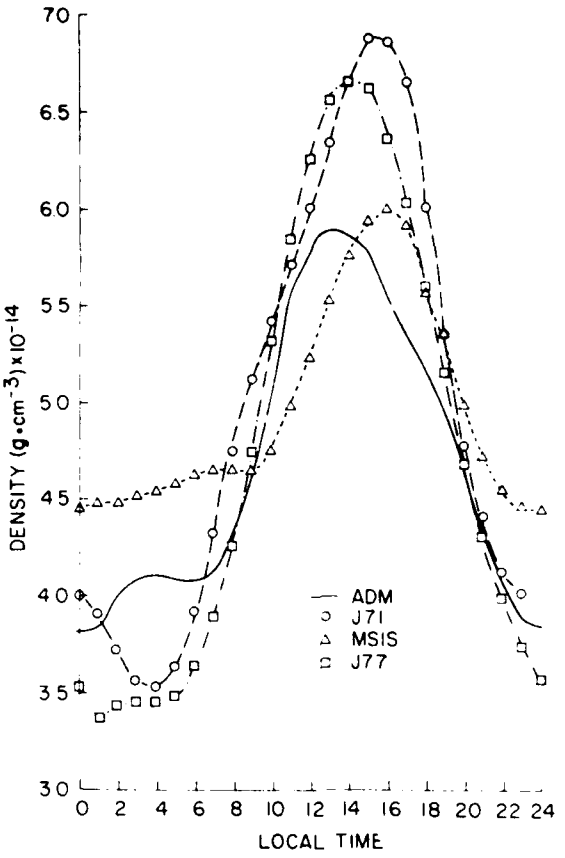

Figure 10c. Density Variation at 240 km as a Function of Local Time

Table 4. Phase of Semidiurnal Variation at 160 km

	Maxima (hr)		Minima (hr)	
ADM	8 1/2	21 1/2	2 1/2	15 1/2
MSIS	9	21	3 1/2	15

Table 5. Amplitude of Semidiurnal Variation at 160 km

	Morning Max / Afternoon Min	Evening Max / Afternoon Min	Morning Max / Morning Min	Evening Max / Morning Min
ADM	1.140	1.130	1.160	1.150
MSIS	1.135	1.157	1.143	1.164

present analysis, the J71 and J77 models significantly overestimate the amplitude of the diurnal bulge at the altitudes studied. The cos λ_{ss} term (Eq. 2) representing the subsolar bulge did not enter the regression analysis at any altitude between 140 to 240 km. Examination of the ADM density distribution as a function of latitude (for LT = 1500 hr) during the solstices shows maximum density values at auroral, rather than subsolar, latitudes in the summer hemisphere. This is assumed to be a consequence of high latitude heat sources.

4.4 Annual Variations

Density variations with annual and subannual periodicities as distinguished from periodic changes connected with the rotation of the earth and sun are a regular feature of the upper atmosphere. They are referred to as the "semiannual variation" and are generally characterized in current models by equinoctial maxima and solstitial minima. At the present time the cause of the semiannual variation is not completely understood. Ching and Chiu[19] have shown that EUV heating has proper characteristics to be important at altitudes above 150 km. Mayr and Volland[20] have shown that sources in addition to EUV heating are required to account fully for this variation. High latitude heat sources, including auroral heating related to the semiannual component of the occurrence of magnetic storms,[21] have been invoked. More data and theoretical analysis are required to develop a comprehensive model of the semiannual variation.

The semiannual density variation at 200 km extracted from the accelerometer data at the equator and north and south poles is shown in Figure 11a. Results are for $F = \bar{F} = 75$, LT = 1500 and $K_p = 0$. Data at corresponding latitudes are given for MSIS and J77 models in Figures 11b and 11c, respectively. Data for J71 are not

19. Ching, B.K., and Chiu, Y.T. (1972) Annual and sub-annual effects of EUV heating-I. Harmonic analysis, Planet. Space Sci. 20:1745.

20. Mayr, H.G., and Volland, H. (1972) Theoretical model for the latitude dependence of the annual and semiannual variations, J. Geophys. Res. 77:6774.

21. Russell, C.T., and McPherron, R.L. (1973) Semiannual variation of geomagnetic activity, J. Geophys. Res. 78:92.

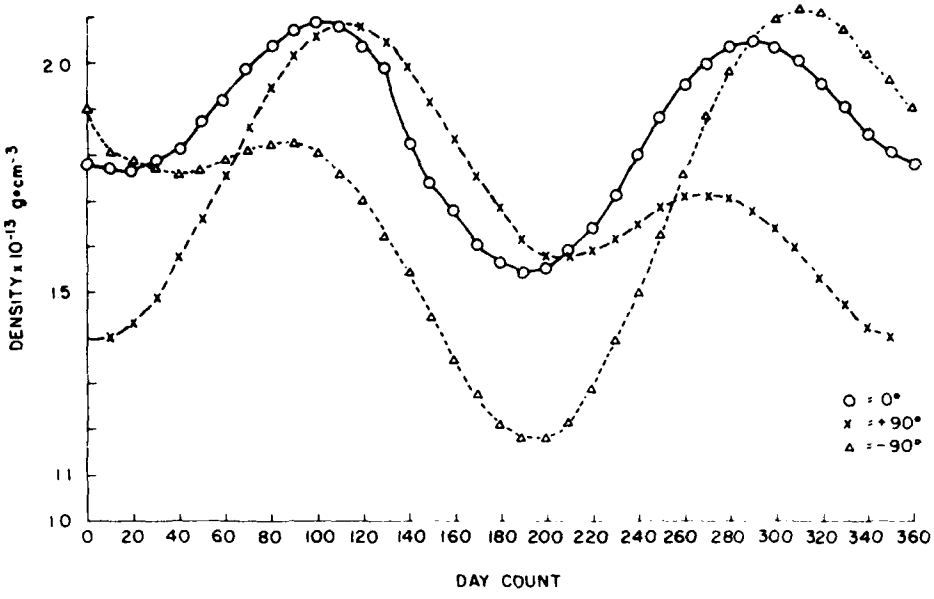

Figure 11a. Density at 200 km vs Day of Year for ADM

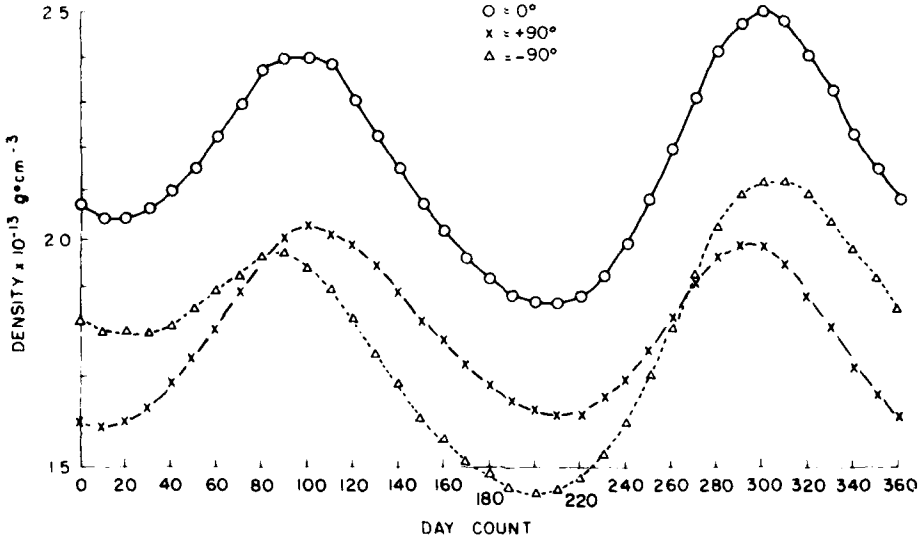

Figure 11b. Density at 200 km vs Day of Year for J77

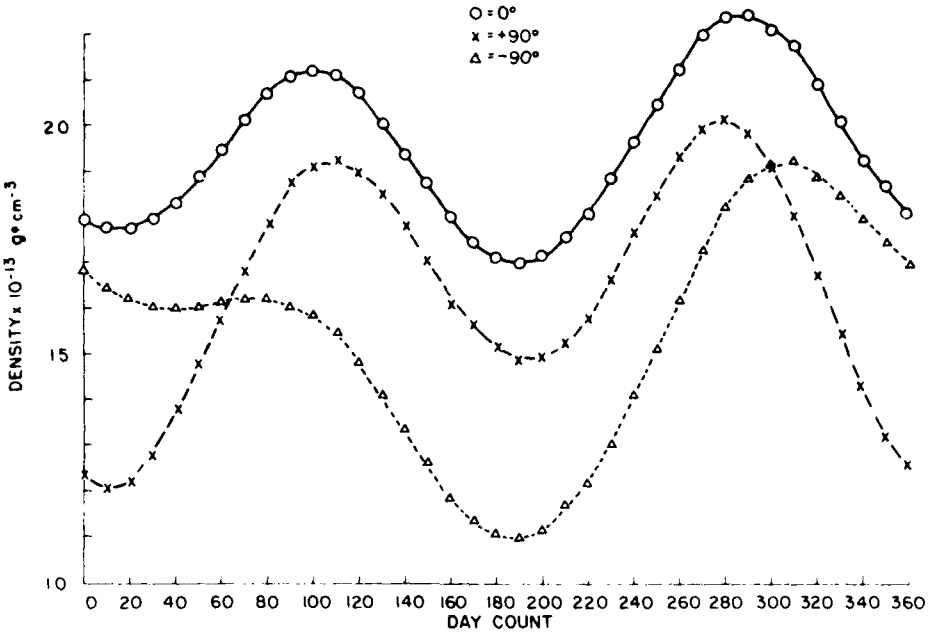

Figure 11c. Density at 200 km vs Day of Year for MSIS

shown, but are essentially the same as for J77. Phases at the three latitudes are summarized in Table 6. Although there are variations in the month of occurrence of some maxima and minima, the columns are labeled "Jan min.," "Apr max.," "July min." and "Oct max." for convenience. In each case, the phases and their variations with latitude are in very good agreement. Although the J77 January minimum occurs 20 days before that of ADM and MSIS at -90°, the curves are quite flat for this case. Therefore, the discrepancy is not significant. A most striking feature of the amplitude of the ADM semiannual variation is the latitudinal behavior of the October maximum. In the southern hemisphere, this maximum is larger than the April maximum. At the equator, the two maxima are nearly equal. At the north pole, the October maximum amplitude is very small. The details of this behavior are qualitatively similar for the other two models depicted in Figures 11b and 11c. The difference between the hemispheres occurs because the seasonal effect is in phase with the annual effect in the southern hemisphere and in opposite phase in the northern hemisphere. To analyze further the derived amplitude structure, ratios have been calculated at -90°, 0°, and +90° for each model for four cases: (1) Apr max/July min, (2) Oct max/July min, (3) Apr max/Jan min and (4) Oct max/Jan min. These results are summarized in Table 7. At the

Table 6. **Phase of Semiannual Variation at 200 km**

Latitude	Model	Jan Min (day)	Apr Max (day)	July Min (day)	Oct Max (day)
-90°	ADM	40	90	195	310
	J77	20	90	200	310
	MSIS	40	80	190	310
0°	ADM	20	100	190	290
	J77	15	100	205	300
	MSIS	20	100	190	290
+90°	ADM	5	110	205	270
	J77	10	100	210	290
	MSIS	10	110	190	280

Table 7. Amplitude of Semiannual Variation at 200 km

Latitude	Model	Apr Max July Min	Oct Max July Min	Apr Max Jan Min	Oct Max Jan Min
-90°	ADM	1.55	1.81	1.03	1.20
	J77	1.36	1.48	1.09	1.19
	MSIS	1.47	1.73	1.01	1.19
0°	ADM	1.36	1.33	1.18	1.16
	J77	1.29	1.34	1.17	1.22
	MSIS	1.24	1.31	1.20	1.27
+90°	ADM	1.33	1.10	1.50	1.23
	J77	1.25	1.23	1.28	1.25
	MSIS	1.29	1.35	1.58	1.36

equator, all three model amplitudes are in excellent agreement with values within ±1.5 percent for cases 2 and 3, and within ±6 percent for cases 1 and 4. At -90°, the ADM amplitude structure agrees more closely with MSIS. For the north pole data, the comparison results are less consistent. All models show an amplitude of 29 ±4 percent for case 1. The ADM amplitude agrees better with MSIS for case 3 and with J77 for case 4. The ADM Oct max/July min (case 2) amplitude (10 percent) is lower than both J77 (23 percent) and MSIS (35 percent). Therefore, the ADM October maximum exhibits a strong hemispheric dependence with a significant decrease in amplitude from the south to north pole.

Global density distributions at 160, 200, and 240 km are summarized as a function of latitude and day of year in Figures 12a, b, c, respectively. These contour maps are for the conditions $F = \bar{F} = 75$, LT = 1500 and $K_p = 0$. Numbers on each plot indicate a density value relative to the average density (for all conditions) at that altitude. Examination of these figures shows that the characteristics of the semiannual variation, particularly the low amplitude of the northern hemisphere October maximum, are similar at all three altitudes.

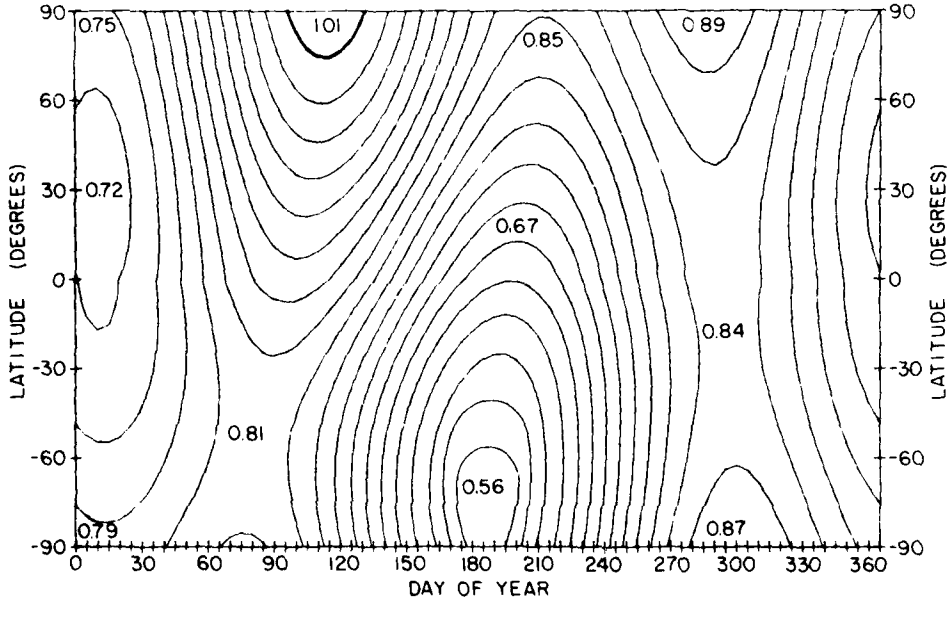

Figure 12a. Contour Map of Density at 160 km vs Latitude and Day of Year, for $F = \bar{F} = 75$, LT = 1500 hr and $K_p = 0$

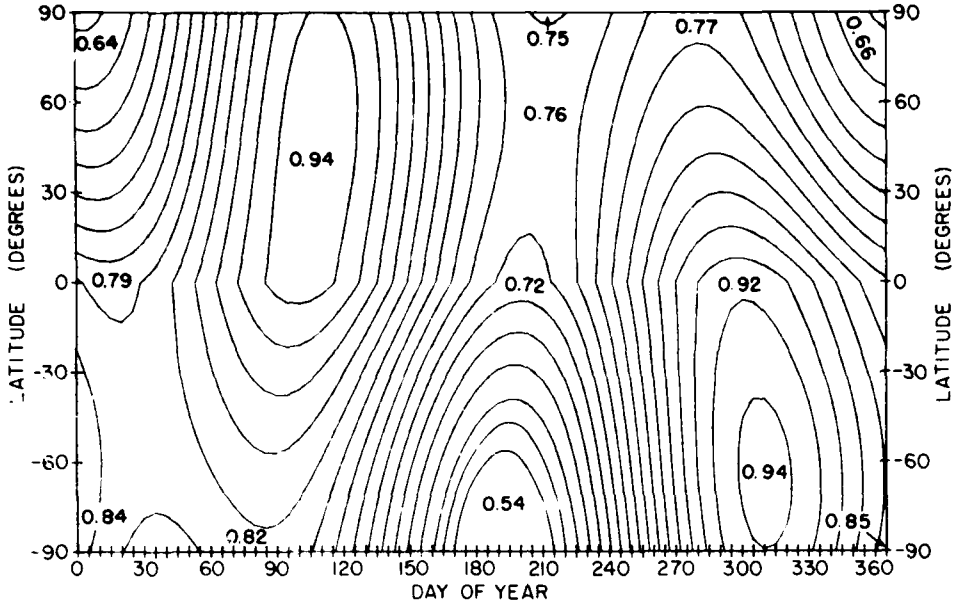

Figure 12b. Contour Map of Density at 200 km vs Latitude and Day of Year, for $F = \bar{F} = 75$, LT = 1500 hr and $K_p = 0$

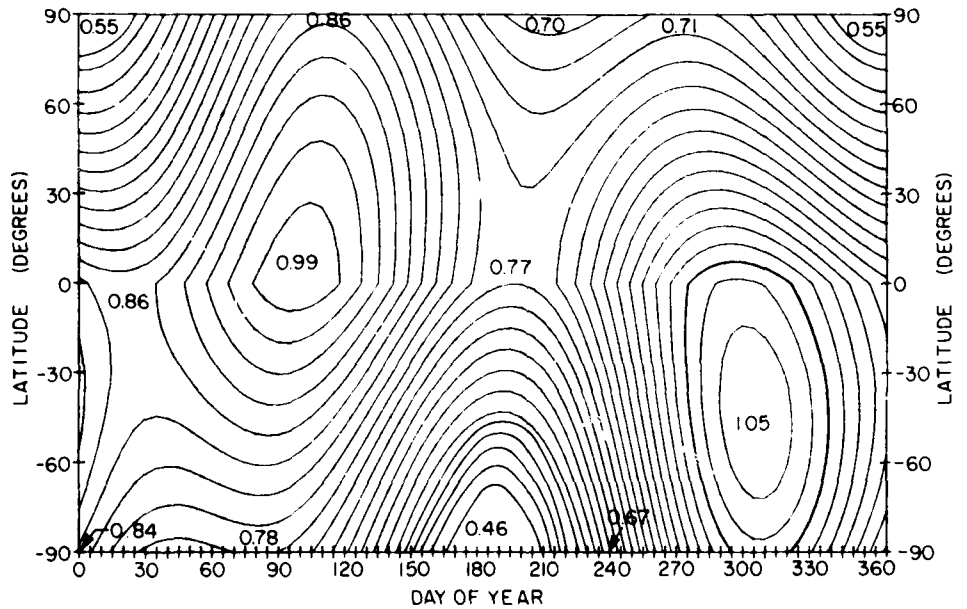

Figure 12c. Contour Map of Density at 240 km vs Latitude and Day of Year, for $F = \bar{F} = 75$, LT = 1500 hr and $K_p = 0$

Composition data at 200 km from MSIS at -90°, 0 and +90° are shown in Figure 13. Nitrogen (N_2) and atomic oxygen (O) display different behavior as a function of latitude and day of year. While atomic oxygen has a pronounced semiannual variation at +90°, N_2 has one maximum in May. However, composition effects are not distinguishable in accelerometer data. Composition measurements from mass spectrometers on AE-D should aid in explaining the relative concentrations of O and N_2 leading to the low total density values for the northern hemisphere fall maximum. However, the cause of this phenomenon and whether it is peculiar to low solar flux conditions require additional data and theoretical analysis.

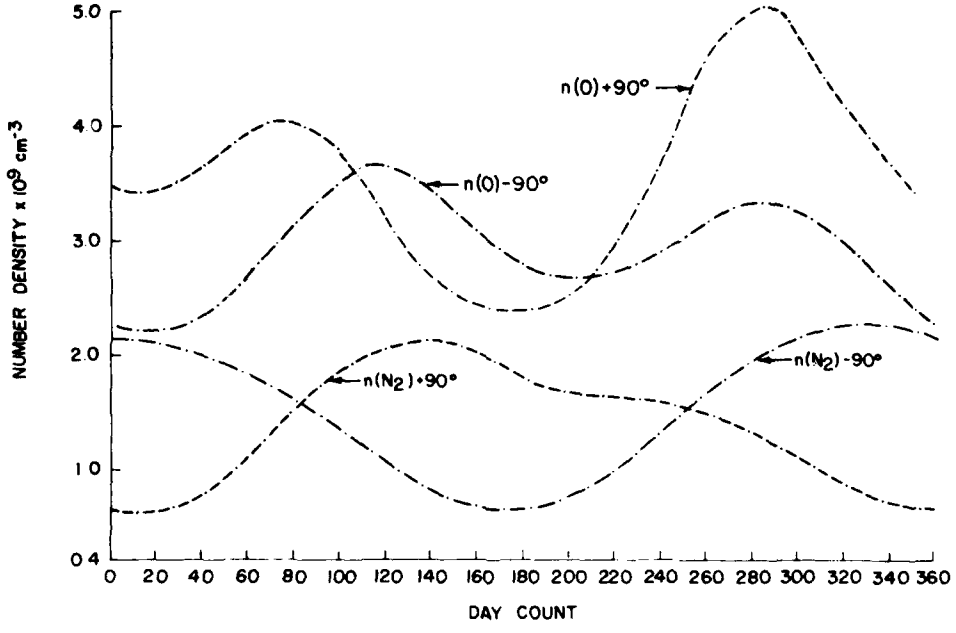

Figure 13. Composition Data at 200 km vs Day of Year for MSIS

4.5 Statistical Evaluation of Models

To investigate the over-all accuracy of models, statistical comparisons to the data base were made. The first and second moments of R (ratio of measured data to model) are determined respectively by:

$$\bar{R} = \sum_{i=1}^{N} \frac{R_i}{N} \tag{4}$$

and

$$\sigma = \left[\sum_{i=1}^{N} \frac{(R_i - \bar{R})^2}{N-1} \right]^{\frac{1}{2}} \tag{5}$$

where $\bar{R}$ is the mean value, R_i is the ratio of the i^{th} density measurement to the model, N the number of points and σ the standard deviation.

The measured density values from each individual set of satellite data (at all altitudes) were first statistically analyzed in relation to the J71, J77, and MSIS models. Table 8 summarizes values of N, R and σ for each satellite. The mean values are within ±2 percent for each set with respect to the J71 and J77 models and within ±3 percent for the MSIS model. This demonstrates the consistency of the data sets for modeling purposes. Further, it implies that the average drag coefficient for S3-1 did not differ significantly from that of the AE satellites; S3-1 was trapezoidal-shaped while the AE's were squat cylinders. For all four satellites a constant value of $C_D = 2.2$ was used. Standard deviations in Table 8 fall in the range 0.14 to 0.18 for all cases. The MSIS provides, for the average conditions of this data base, a slightly better depiction of atmospheric variability. The percentage standard deviation for each model, averaged over the four sets of satellite data are: MSIS = 14.7, J71 = 15.1 and J77 = 15.8.

Table 8. Ratio of Total Mass Density to Model Density for Satellites S3-1, AE-C, -D and -E for Altitudes 140-240 km

		J71		J77		MSIS	
	N	$\bar{R}$	σ	$\bar{R}$	σ	$\bar{R}$	σ
S3-1	27,315	1.06	0.15	1.04	0.15	1.00	0.14
AE-C	57,716	1.09	0.16	1.05	0.17	1.05	0.15
AE-D	28,668	1.05	0.16	1.00	0.15	0.98	0.16
AE-E	34,364	1.08	0.18	1.03	0.18	1.01	0.15

Evaluation of $\bar{R}$ and σ for ADM was made at each 5-km interval, using the combined four data sets. Table 9 shows a comparison of ADM and the other three models at the altitude of 200 km. The ADM percentage standard deviation is 1.9 percent less than that of MSIS, 2.7 percent less than J71, and 3.4 percent less

Table 9. Comparison of Model Density Ratios for All Satellite Data at 200 km

	$\bar{R}$	σ
ADM	1.00	0.12
J71	1.09	0.16
J77	1.04	0.16
MSIS	1.01	0.14
Total number of points = 8747		

than J77. The calculated standard deviation for ADM must presently be viewed as an internal test of the consistency between the mathematical representation and the data set used for model development. The test of the model is its ability to represent data not used in its construction. An evaluation of a preliminary version of this model with available data obtained over a 20-day period from a high inclination satellite did show results consistent with those of Table 9. More extensive tests are planned using a larger data set.

5. CONCLUSIONS

Density variations in the lower thermosphere related to solar flux, geomagnetic activity, local time, latitude and the semiannual effect have been determined from the S3-1 and AE-C, -D, and -E accelerometer data base, using multiple linear regression analysis. The resulting Accelerometer Density Model is believed to provide a better representation of the low-altitude satellite aerodynamic environment than other global density models. The major results of this study are:

1. The density is more variable with the solar cycle dependent EUV flux as represented by $\bar{F}_{10.7}$ than predicted by current models.

2. Geomagnetic activity variations exhibit a latitude dependence with a maximum at high latitudes.

3. The subsolar (diurnal tide) bulge is dominated at altitudes below ~200 km by the semidiurnal tide. Also, density values maximize in the summer hemisphere at auroral latitudes rather than at low latitudes in the vicinity of the subsolar point. This is consistent with a high-latitude heat source that is effective even during geomagnetically quiet times.

4. A strong hemispherical asymmetry for the October maximum characterizes the semiannual variation. The October maximum has its greatest amplitude at the south pole and its amplitude decreases from the south pole to the north pole.

5. Statistically, the ADM standard deviation is about 2 to 3 percent lower than that of the other models tested.

The accelerometer data base has been used to develop an improved model of lower thermospheric density variations. This model is applicable to low solar flux conditions and is based largely on data at low and middle latitudes. Data obtained from the ROCA and SETA accelerometer experiments on high inclination satellites have been obtained during periods of moderate to high solar flux. Incorporation of these results into the present data base will improve the accuracy and extend the applicability of the present model.

References

1. Forbes, J.M., and Garrett, H.B. (1975) Variations in the atmospheric neutral density at 145 km, Planet. Space Sci. 23:1399.

2. Marcos, F.A., Garrett, H.B., Champion, K.S.W., and Forbes, J.M. (1977) Density variations in the lower thermosphere from analysis of the AE-C accelerometer measurements, Planet. Space Sci. 25:499.

3. Marcos, F.A., and Champion, K.S.W. (1979) Empirical model of lower thermospheric density for low solar flux and quiet geomagnetic conditions, Space Research 19:89.

4. Jacchia, L.G. (1971) Revised Static Models of the Thermosphere and Exosphere with Empirical Temperature Profiles, Spec. Rept. 332, Smithsonian Astrophys. Observatory, Cambridge, Massachusetts.

5. Jacchia, L.G. (1977) Thermospheric Temperature Density and Composition: New Models, Special Rept. 375, Smithsonian Astrophys. Observatory, Cambridge, Massachusetts.

6. Hedin, A.E., Salah, J.E., Evans, J.V., Reber, C.A., Newton, G.P., Spencer, N.W., Kayser, D.C., Alcayde, D., Bauer, P., Cogger, L., and McClure, J.P. (1977) A global thermospheric model based on mass spectrometer and incoherent scatter data, MSIS 1, N_2 density and temperature, J. Geophys. Res. 82:2139.

7. Marcos, F.A., and Champion, K.S.W. (1979) Satellite Density Measurements with a Rotatable Calibration Accelerometer (ROCA), AFGL-TR-79-0005, ADA 069740.

8. Marcos, F.A., and Swift, E.R. (1982) Application of the Satellite Triaxial Accelerometer to Atmospheric Density and Wind Studies, AFGL-TR-82-0091).

9. Marcos, F.A., McInerney, R.E., and Fioretti, R.W. (1978) Variability of the Lower Thermosphere Determined from Satellite Accelerometer Data, AFGL-TR-78-0134, ADA 058982, Air Force Geophysics Laboratory, Hanscom AFB, Massachusetts.

10. Hinteregger, H.E. (1979) Development of solar cycle 21 observed in EUV spectrum and atmospheric absorption, J. Geophys. Res. 84:1933.

11. Mayr, H.G., Harris, I., and Spencer, N.W. (1978) Some properties of upper atmosphere dynamics, Rev. Geophys. Space Phys. 16:539.

12. Cage, A.L., and Zawalick, E.J. (1972) A Discussion of Geomagnetic Indices K_p and A_p, 1932 to 1971, AFCRL-72-0693, AD 756828.

13. Hedin, A.E., Spencer, N.W., Mayr, H.G., and Porter, H.S. (1981) Semi-empirical modelling of thermospheric magnetic storms, J. Geophys. Res. 86:3151.

14. Porter, H.S., Mayr, H.G., and Hedin, A.E. (1981) An analytic formulation for heating source memory in the thermospheric composition, J. Geophys. Res. 86:3555.

15. Jacchia, L.G., and Slowey, J.W. (1981) Analysis of Data for the Development of Density and Composition Models of the Upper Atmosphere, AFGL-TR-81-0230, ADA 106420.

16. Forbes, J.M., and Marcos, F.A. (1979) Tidal variations in total mass density as derived from the AE-E Mesa experiment, J. Geophys. Res. 84:31.

17. Forbes, J.M. (1978) Tidal variations in O, O_2, N_2, Ar, He and H, J. Geophys. Res. 83:3691.

18. Forbes, J.M., and Marcos, F.A. (1980) Seasonal-latitudinal tidal structure, of O, N_2 and total mass density in the thermosphere, J. Geophys. Res. 85:3489.

19. Ching, B.K., and Chiu, Y.T. (1972) Annual and sub-annual effects of EUV heating-I. Harmonic analysis, Planet. Space Sci. 20:1745.

20. Mayr, H.G., and Volland, H. (1972) Theoretical model for the latitude dependence of the annual and semiannual variations, J. Geophys. Res. 77:6774.

21. Russell, C.T., and McPherron, R.L. (1973) Semiannual variation of geomagnetic activity, J. Geophys. Res. 78:92.

M-4

11-82

END